Monthly Notices
of the
ROYAL ASTRONOMICAL SOCIETY

MNRAS **474,** 4795–4809 (2018)
Advance Access publication 2017 November 24

doi:10.1093/mnras/stx3023

A dearth of small particles in the transiting material around the white dwarf WD 1145+017

S. Xu(许偲艺),[1⋆] S. Rappaport,[2⋆] R. van Lieshout,[3⋆] A. Vanderburg,[4] B. Gary,[5] N. Hallakoun,[6,1] V. D. Ivanov,[1,7] M. C. Wyatt,[3] J. DeVore,[8] D. Bayliss,[9] J. Bento,[10] A. Bieryla,[4] A. Cameron,[11] J. M. Cann,[12] B. Croll,[13] K. A. Collins,[4] P. A. Dalba,[13] J. Debes,[14] D. Doyle,[15] P. Dufour,[16] J. Ely,[17] N. Espinoza,[18] M. D. Joner,[19] M. Jura,[20] T. Kaye,[21] J. L. McClain,[15,22] P. Muirhead,[13] E. Palle,[23,24] P. A. Panka,[12] J. Provencal,[25] S. Randall,[1] J. E. Rodriguez,[4] J. Scarborough,[15] R. Sefako,[26] A. Shporer,[27] W. Strickland,[15] G. Zhou[4] and B. Zuckerman[20]

Affiliations are listed at the end of the paper

Accepted 2017 November 14. Received 2017 November 14; in original form 2017 August 9

ABSTRACT

White dwarf WD 1145+017 is orbited by several clouds of dust, possibly emanating from actively disintegrating bodies. These dust clouds reveal themselves through deep, broad, and evolving transits in the star's light curve. Here, we report two epochs of multiwavelength photometric observations of WD 1145+017, including several filters in the optical, K_s and 4.5 μm bands in 2016 and 2017. The observed transit depths are different at these wavelengths. However, after correcting for excess dust emission at K_s and 4.5 μm, we find the transit depths for the white dwarf itself are the same at all wavelengths, at least to within the observational uncertainties of ∼5–10 per cent. From this surprising result, and under the assumption of low optical depth dust clouds, we conclude that there is a deficit of small particles (with radii $s \lesssim 1.5$ μm) in the transiting material. We propose a model wherein only large particles can survive the high equilibrium temperature environment corresponding to 4.5 h orbital periods around WD 1145+017, while small particles sublimate rapidly. In addition, we evaluate dust models that are permitted by our measurements of infrared emission.

Key words: eclipses – minor planets, asteroids: general – stars: individual: WD 1145+017 – white dwarfs.

1 INTRODUCTION

Recent studies show that relic planetary systems or their debris are widespread around white dwarfs. About 25–50 per cent of white dwarfs show 'pollution' from elements heavier than helium in their atmospheres (Zuckerman et al. 2003, 2010; Koester, Gänsicke & Farihi 2014). The most heavily polluted white dwarfs often display excess infrared emission from a dust disc within the white dwarf's tidal radius (e.g. von Hippel et al. 2007; Farihi, Jura & Zuckerman 2009). About 20 per cent of these dusty white dwarfs also display double-peaked calcium infrared triplet emission lines from orbiting gas debris which spatially coincides with the dust disc (e.g. Gänsicke et al. 2006; Brinkworth et al. 2009; Melis et al. 2010). A widely accepted model is that the white dwarfs are accreting debris of disrupted minor planets that survived the post-main-sequence evolution of the white-dwarf progenitor. These minor planets would have been perturbed into the white dwarf's tidal radius and subsequently disrupted (Debes & Sigurdsson 2002; Jura 2003). Therefore, high-resolution spectroscopic observations of the heavily polluted white dwarfs can uniquely reveal the bulk chemical compositions of these extrasolar minor planets (Zuckerman et al. 2007; Jura & Young 2014).

No evidence, however, for such a disintegrating minor planet has ever been directly identified until relatively recently. WD 1145+017 happened to be observed by the K2 mission (in Campaign 1), and it was observed to display transits with multiple periods ranging from 4.5 to 4.9 h (Vanderburg et al. 2015). Follow-up observations came quickly (e.g. Gänsicke et al. 2016; Rappaport et al. 2016; Croll et al. 2017; Gary et al. 2017) and found that the transit durations range from ∼3 min to as long as an hour – much longer than expected for a solid body (Vanderburg et al. 2015). The transits are inferred to be caused by the passage of dust clouds rather than solid

⋆ E-mail: sxu@gemini.edu (SX); sar@mit.edu (SR); lieshout@ast.cam.ac.uk (RvL)

bodies. Presumably each periodicity represents the orbit of a different underlying body that supplies the dusty effluents. In turn, these bodies are currently hypothesized to be fragments from the tidal disruption of an asteroidal parent body. At these orbital periods, all the orbiting objects lie close to the white dwarf's tidal radius. The transit profiles are variable, asymmetric, and display depths up to 60 per cent (e.g. Gänsicke et al. 2016; Rappaport et al. 2016; Croll et al. 2017; Gary et al. 2017); they are morphologically similar to transits of disintegrating planets around main-sequence stars (e.g. Rappaport et al. 2012). On a time-scale of a few weeks, there can be significant evolution of the transit shape and depth (e.g. Gänsicke et al. 2016; Croll et al. 2017; Gary et al. 2017). The origin, creation mechanism, and lifetimes of these orbiting bodies are currently uncertain at best, with inferred masses in the range of 10^{17}–10^{24} g (Vanderburg et al. 2015; Rappaport et al. 2016). Additional dynamical simulations support the statement that the orbiting objects should be no more massive than Ceres (Gurri, Veras & Gänsicke 2017). In order to produce the observed transit features, the disintegrating objects are likely to be in circular orbits and also differentiated (Veras et al. 2017).

When observed with the Keck Telescope, WD 1145+017 was found to display photospheric absorption lines from 11 elements heavier then helium, making it one of the most heavily polluted white dwarfs known (Xu et al. 2016). In addition, a uniquely rich set of circumstellar absorption lines from seven elements was detected. These lines tend to have large velocity dispersions ($\sim$300 km s^{-1}), and may well be associated with gas orbiting near the white dwarf (i.e. at distances of $\sim$5–15 white dwarf radii; Redfield et al. 2017; Vanderburg & Rappaport 2018). The circumstellar line profiles have changed significantly since their original discovery (Redfield et al. 2017). In addition, WD 1145+017 displays infrared excess from orbiting dust particles (Vanderburg et al. 2015).

There have been several attempts with multiwavelength observations to constrain the properties of the transiting material. If the transits are caused by optically thin dust passing in front of the star, the transit depths should be wavelength dependent due to the wavelength dependence behaviours of Mie scattering cross-sections. From simultaneous *V*- and *R*-band observations, Croll et al. (2017) concluded that the particle radii must be larger than 0.15 μm or smaller than 0.06 μm. Alonso et al. (2016) reported observations from 4800 to 9200 Å and found no difference in the transit depth across that wavelength range. They concluded that particle sizes less than 0.5 μm can be excluded for the common minerals. Zhou et al. (2016) extended the observations to *J* band and still found no wavelength dependence of the transits. They placed a 2σ lower limit on the particle size of 0.8 μm. The first detection of a wavelength-dependent transit was recently reported in Hallakoun et al. (2017), which features 'bluing – transits are shallower in the u' band than those in the r' band, in contrast to the usual expectation in a dusty environment. After exploring different scenarios, they concluded that the most likely explanation is the reduced absorption of circumstellar lines during transits.

In this work, we extend the photometric observations to 4.5 μm. This paper is organized as follows. In Section 2, we present the details of our observations and the data analysis methods. In Section 3, we derive transit depth ratios and find that they are consistent at all the observed wavelengths. We interpret this as a result of the prevalence of large grains in Section 4. We explore a model that would explain the dearth of small grains in Section 5. The connection between the transiting material and the infrared excess is discussed in Section 6 and the conclusion is given in Section 7.

2 OBSERVATIONS AND DATA REDUCTION

We have carried out two epochs of multiwavelength photometric observations that cover optical to 4.5 μm during both 2016 March 28–29 and 2017 April 4–5. The observing logs are listed in Table 1 and the light curves are shown in Figs 1 and 2. We describe the observations and data reduction methods in the following section.

2.1 WET and Perkins: optical

For the optical observation in 2016, we used the 0.6m Paul and Jane Meyer Observatory Telescope in the Whole Earth Telescope (WET) network with the BG 40 filter. Data reduction was performed following the procedures developed for the WET observations (Provencal et al. 2012). There were passing (terrestrial) clouds, which caused some gaps and increased scatter in certain portion of the light curve, as shown in Fig. 1.

During the 2017 observing run, we arranged observations with several optical telescopes. The details of these observations are described in Appendix A. Here, we focus on data taken on the 1.8-m Perkins telescope at the Lowell Observatory using the Perkins Re-Imaging System (Janes et al. 2004), which has the best data quality. The observation was designed following previous WD 1145+017 observations (Croll et al. 2017). The observing conditions were moderately good. Seeing was around 3.0 arcsec and there were thin cirrus clouds at the beginning of the observation, which developed substantially throughout the night. Data reduction was performed following a custom pipeline (Dalba & Muirhead 2016; Dalba et al. 2017).

2.2 VLT/HAWK-I: K_s

On 2016 March 28–29, WD 1145+017 was monitored in K_s band with the HAWK-I (High Acuity Wide field *K*-band Imager; Pirard et al. 2004) at the Very Large Telescope (VLT). The camera is equipped with four HAWAII 2RG 2048 × 2048 detectors, with a plate scale of $\sim$0.106 arcsec pixel^{-1}. We used the *Fast Jitter* mode that allows one to window down the detectors, greatly reducing the readout overheads. Following similar procedures outlined in Cáceres et al. (2011), we applied windows of 128 × 256 pixels per detector stripe. We recorded a sequence of blocks, each consisting of 60 exposures with 15 s integration time. Throughout the observations, we kept the nearby star ULAS J114829.42+012707.6 ($K_s = 16.678 \pm 0.042$) on the same detector as the science target to provide a flux reference. The weather conditions were moderate and there were thin clouds passing by during the observations. The DIMM seeing was about 0.55 arcsec in the optical.

Individual images were dark-subtracted and flat-field corrected with sky flats taken immediately after the observation. Aperture photometry was performed with aperture radii of 5, 7, and 10 pixels. The sky background was estimated from an annulus of between 10 and 20 pixels. We found that the light curve from the 7 pixel (0.75 arcsec) radius aperture has the best quality and use this light curve for the rest of our analysis. Both the target light curve and the reference star light curve were normalized by dividing by a constant, as shown in Fig. 3.

We repeated the observations with HAWK-I on 2017 April 4–5 with a similar set-up. The observing conditions were better: clear sky with optical seeing at the beginning of 1.0 arcsec, which decreased to 0.5 arcsec towards the end of the observation. We started the observations with a block of 60 exposures with 15 s integration each. We repeated this block five times before noticing that the

Table 1. Observing logs.

Instrument	Central wavelength	Observing time (UT)	Exposure time (s)
		2016	
Meyer	0.48 μm	Mar 28, 21:00–Mar 29, 04:37[a]	60
VLT/HAWK-I	2.1 μm (K_s)	Mar 29, 03:43–06:28	15
Spitzer/IRAC	4.5 μm	Mar 28, 22:18–Mar 29, 06:04	30
		2017	
Perkins/R	0.65 μm	Apr 5, 03:12–09:50	45
VLT/HAWK-I	2.1 μm (K_s)	Apr 5, 00:33–07:19	15, 30[b]
Spitzer/IRAC	4.5 μm	Apr 4, 22:42–Apr 5, 08:33	30

Notes. [a]There are some gaps in the light curve due to passing clouds.
[b]The first set of observations (∼75 min) was executed in 15 s exposure time.

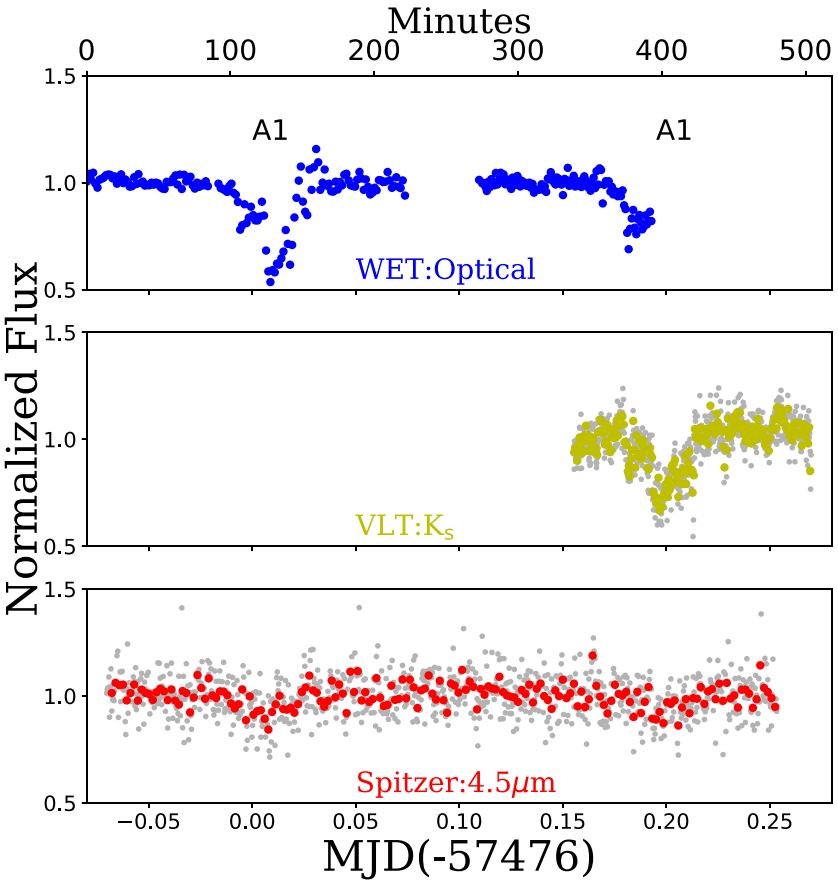

Figure 1. The light curves from all the observations on 2016 March 28–29. There was one main transit feature during a full period of 270 min and we denote it as A1. For the K_s and 4.5 μm band observations, the grey dots represent individual measurements. The yellow dots are smoothed with every three data points and the red dots are smoothed every five data points.

target was not visible in the guider. Out of concern that the target had drifted out of the small field of view, we stopped the sequence, reacquired the target, and increased the exposure time to 30 s. After that, we observed in blocks consisting of 30 exposures with 30 s integration times until the end of the observation.

Data reduction was performed following the same method as for the 2016 data set. We adopted an aperture radius of 8 pixels (0.85 arcsec), and a sky annulus between 10 and 20 pixels for aperture photometry. In retrospect, our target did not disappear around 57848.08 (MJD); in fact, there was a deep transit, which made the target difficult to see in individual images. Because the data quality was better with 30-s exposure time, we focus on these for the following analysis.

2.3 *Spitzer*/IRAC: 4.5 μm

We were awarded time with the Infrared Array Camera (IRAC; Fazio et al. 2004) on the *Spitzer Space Telescope* under a Director's Discretionary Time (DDT) programme to observe WD 1145+017 simultaneously with the VLT on 2016 March 28–29. The observation was designed following 'Advice for designing high precision photometry observations'.[1] The science observations consisted of 900 exposures of 30 s each in the 4.5 μm filter in stare mode. The readout mode was full array. The target was put in the well-characterized pixel (sweet spot). Before the science observation,

[1] http://irachpp.spitzer.caltech.edu/page/Obs%20Planning

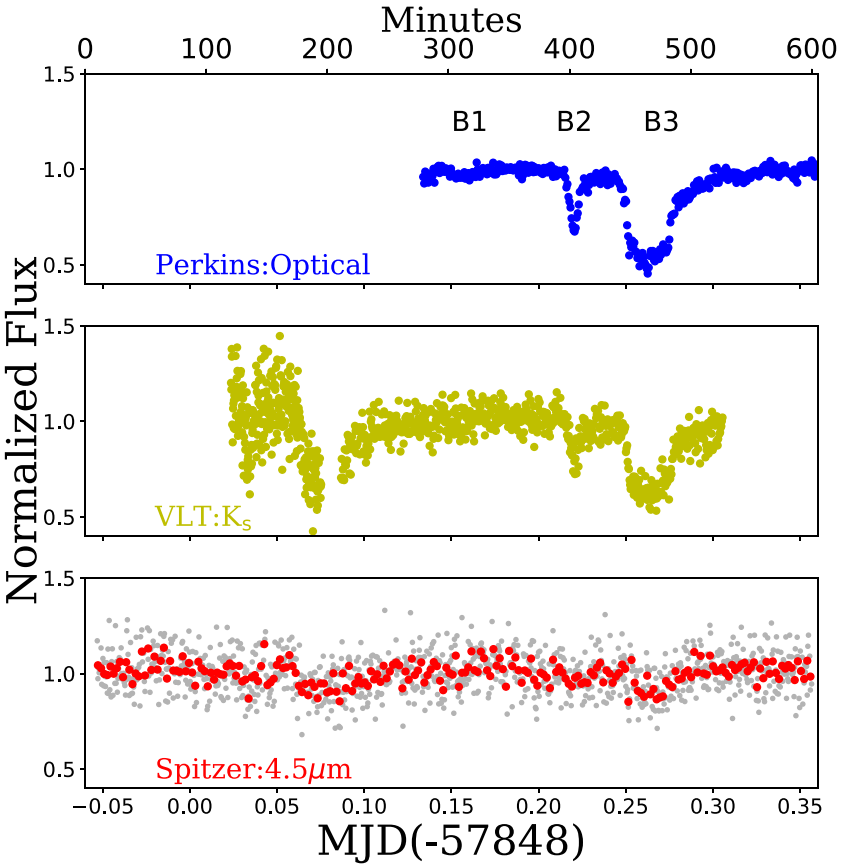

Figure 2. The light curves from all the observations on 2017 April 4–5. There are three main transit features in a full period of 270 min, denoted as B1, B2, and B3. All the notations are the same as those in Fig. 1.

we arranged a 30 min exposure to eliminate the initial drift of the instrument (Grillmair et al. 2012). We also included a 10 min post-observation with the same set-up as the pre-observation.

For the data reduction, we started with the CBCD (Corrected Basic Calibrated Data) files, which are flux-calibrated and artefact-corrected files from the pipeline (IRAC Instrument Handbook). We excluded a few frames when there was a cosmic ray close to the target. The pre-observation and post-observation frames were median combined and smoothed to create a localized dark frame, which was then subtracted from all CBCD files to remove any residual patterns. To produce the light curve, we used codes that are publicly available for IRAC high-precision photometry.[2] The IDL program BOX_CENTROIDER.PRO was used to locate the position of our target in each exposure. We found the average target position to be X = 24.08 ± 0.07, Y = 232.18 ± 0.08, which is very close to the sweet spot at X = 24.0, Y = 232.0. These positions were used as input parameters for aperture photometry in APER.PRO, where an aperture radius of 2 pixels and a sky annulus of 12–20 pixels were used. The last step was to correct for the intrapixel gain with a pre-gridded pixel map in IRACPC_PMAP_CORR.PRO. The normalization was done by dividing the light curve by a constant.

The same set of observations was repeated on 2017 April 4–5. A total of 1140 exposures for science observations were obtained with 30 s exposure time each. The observation covered more than two full periods. The average centroid position for the target was 24.08 ± 0.08 in X and 232.31 ± 0.09 in Y. We followed the same data reduction procedures as for the 2016 data set.

In order to measure the absolute flux in 4.5 μm, we took the median value of the measured out-of-transit flux. After aperture correction, we found that the flux was 55.0 ± 2.3 μJy and 55.5 ± 2.5 μJy in 2016 and 2017, respectively. Evidently, the infrared excess remained stable. We took the average of these numbers and also included a conservative 5 per cent calibration uncertainty for IRAC, as found by previous dusty white dwarf studies (Jura, Farihi & Zuckerman 2007b). The final flux is 55.0 ± 3.2 μJy at 4.5 μm, which is consistent with the *WISE W*-2 flux of 43 ± 14 μJy.

3 TRANSIT DEPTHS IN DIFFERENT WAVELENGTHS

3.1 The observed transit depth

In this section, we compare the transit depths at the different observed wavelengths. Some of the observations cover more than one full orbital period, so we folded the light curve about a period of 269.47 min (Gary et al. 2017). This phase folding is unlikely to affect our analysis because typically, there is little evolution in the light curve on an orbital time-scale (e.g. Gary et al. 2017). We confirmed this with our 2017 April ground-based observations, which spanned the full ∼10 h *Spitzer* observations and showed only negligible evolution of the transit shapes and depths over the course of the observations (see Appendix A).

[2] http://irachpp.spitzer.caltech.edu/page/contrib

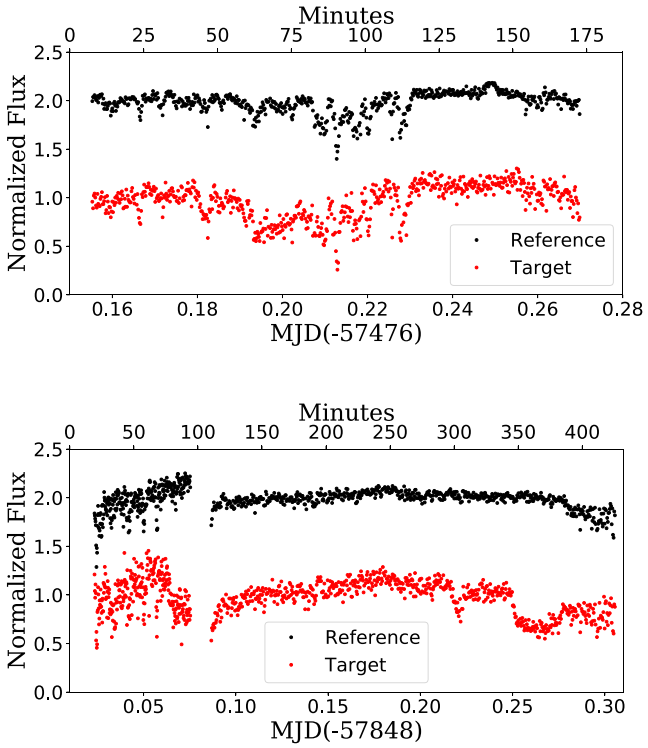

Figure 3. K_s band light curve of WD 1145+017 from the HAWK-I on the VLT. Red dots are the normalized flux for our target WD 1145+017 while black dots are for the reference star ULAS J114829.42+012707.6. For clarity, the black dots are offset by 1.0 from the red dots. The top panel is for the 2016 data set, during mediocre weather conditions with passing clouds; the bottom panel is for the 2017 data set with good weather conditions.

For both the 2016 and 2017 data sets, we start with the optical light curve, which has the lowest point-to-point scatter. Following previous work of fitting asymmetric transit features (e.g. Rappaport et al. 2014; Zhou et al. 2016; Croll et al. 2017; Gary et al. 2017), we model the transits of WD 1145+017 as a sum of asymmetric hyperbolic secant (AHS) functions:

$$f(p) = f_0\ \left[1 - f_{\rm dip}(p)\right] \equiv f_0\ \left(1 - \sum_i \frac{2f_{\rm i}}{{\rm e}^{\frac{p-p_i}{\phi_{i1}}} + {\rm e}^{-\frac{p-pi}{\phi_{i2}}}}\right), \quad (1)$$

where $f(p)$ represents the normalized light curve, f_0 fits the continuum level, and $f_{\rm dip}(p)$ is the fractional flux change during the asymmetric transits. In the second term, i represents the number of AHS components needed to provide a good fit to the transit profile (typically $i = 2$–4), p_i represents a phase near the deepest point during a transit, ϕ_{i1} and ϕ_{i2} represent the ingress and egress duration of a transit, respectively.

Assuming the light curves at all the wavelengths have the same shape but different transit depths, we can fit all the light curves with the following form,

$$f_\lambda(p) = f_{\lambda,0}\ \left[1 - D_\lambda\ f_{\rm dip}(p)\right]. \quad (2)$$

There are only two free parameters here, i.e. $f_{\lambda,0}$ and D_λ, while the parameters for $f_{\rm dip}(p)$ can be taken from the best-fitting parameters for the optical light curve. $f_{\lambda,0}$ is used to fit the continuum level and D_λ is the observed transit depth ratio between the wavelength of interest relative to optical.

Our fitting method adopts a Levenberg–Marquardt algorithm to derive a least-squares fit, and the uncertainty comes from the covariance matrix of the best-fitting values. To estimate the uncertainty in the depth of transits in the optical light curve $D_{\rm opt}$, we repeated the fit following equation (2). The observed uncertainty for the transit depth ratios between a given wavelength λ and the optical includes the uncertainty from $D_{\rm opt}$ and the uncertainty from D_λ.

3.1.1 2016 data set

We set the reference time as 57475.95 (MJD) and the phase-folded light curves are shown in Fig. 4. During our observation, there was one main transit feature with a complex shape. We refer to this feature as A1. It was first detected on 2016 January 21 (denoted as 'G6121' in Gary et al. 2017 and 'A1' in Hallakoun et al. 2017). This feature was well covered in the optical, K_s band, 4.5 μm.

For the WET light curve, we used three AHS components for A1 following equation (1) and the best-fitting parameters are listed in Table 2. We fitted all the light curves with the same functional form but different transit depth D with equation (2), with the results listed in Table 3. The observed transit depths are different at all three wavelengths.

3.1.2 2017 data set

We set the reference time as 57848.13 (MJD) and the phase-folded light curves are shown in Fig. 5. There were three main transit features during a full orbital period, denoted as B1, B2, and B3 (see Appendix A for details). The B1 Dip was shallow and not detected in the K_s band nor the *Spitzer* band, due to their relatively low signal-to-noise ratios compared to the optical light curve. Here, we focus on transits B2 and B3, which are better suited for studying the wavelength dependence of the transits. We believe B2 was due to the same orbiting body that produced A1 in 2016 and B3 could be related to some other features observed in the previous season as well (Rappaport et al. 2018).

We followed the same analysis procedures outlined in Section 3.1. We started with the Perkins light curve and used the functional form for $F_{\rm dip}(p)$ to fit the light curves at all the wavelengths. The results are listed in Tables 2 and 3. The values for B2 and B3 are comparable, while the overall uncertainties for B3 are smaller because the transit was deeper and lasted longer.

3.2 Transit depth correction for dust emission

In both data sets, we find that the transit depths of the observed flux are different at all the wavelengths. It is deepest in the optical and shallower at longer wavelengths. There is no change in the transit depth ratios between these two epochs.

Because WD 1145+017 has an infrared excess starting from the K_s band (Vanderburg et al. 2015), this will necessarily dilute the transit signal. To derive the transit depth ratio corrected for the dust emission, we need to use the intrinsic white dwarf flux rather than the measured flux. As a result, the corrected transit depth ratio can be calculated as

$$D_{\rm corr} = \frac{F_{\rm obs}}{F_\star} \times D, \quad (3)$$

where $F_{\rm obs}$ and $F_\star$ represents the measured out-of-transit flux and the expected flux from the white dwarf, respectively. We know that $F_{\rm obs}$ is constant during the two epochs of our observations. Based on the colour of WD 1145+017, we find that $F_\star$ has little extinction from either circumstellar or interstellar material, and therefore $F_\star$

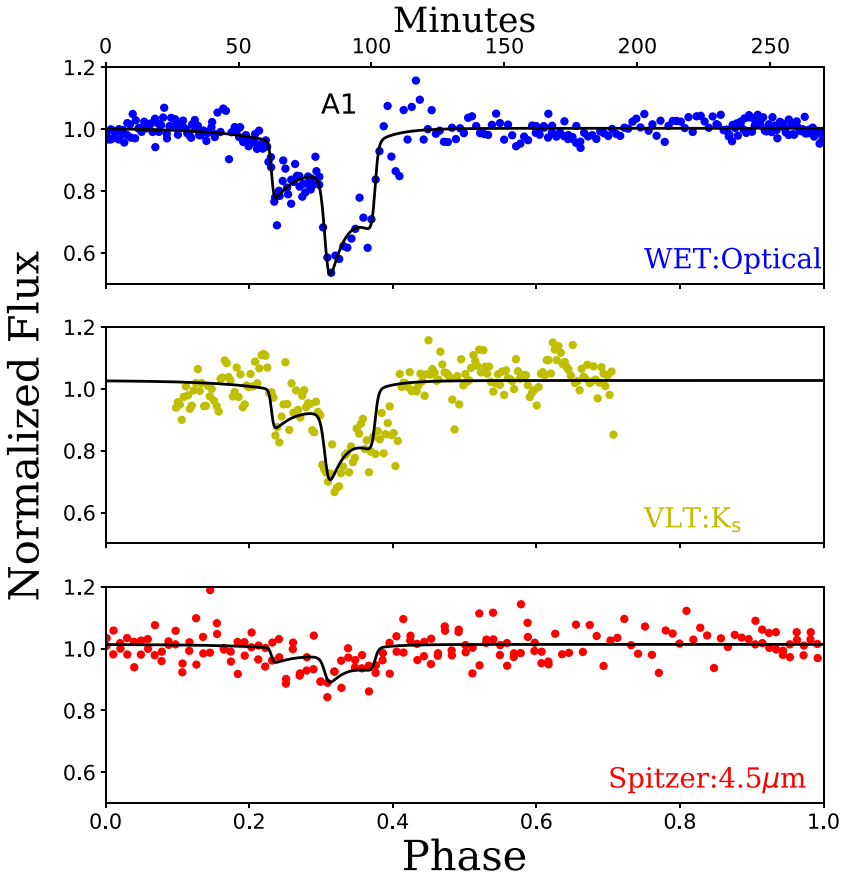

Figure 4. Phase-folded transit light curve in the optical, K_s band, and 4.5 μm, respectively, on 2016 March 28–29. The black line represents the best-fitting models with parameters listed in Tables 2 and 3.

Table 2. Best-fitting parameters for the AHS components of different dip features in the optical band.

Dip	f_0	i	f_i	p_i	ϕ_{i1}	ϕ_{i2}
A1	1.003 ± 0.003	3	0.105 ± 0.012	0.231 ± 0.001	0.048 ± 0.011	0.002 ± 0.001
			0.214 ± 0.025	0.306 ± 0.002	0.028 ± 0.007	0.003 ± 0.001
			0.151 ± 0.023	0.375 ± 0.001	0.002 ± 0.001	0.073 ± 0.010
B1	1.001 ± 0.002	1	0.027 ± 0.006	0.147 ± 0.003	0.003 ± 0.002	0.042 ± 0.013
B2	0.979 ± 0.008	1	0.284 ± 0.026	0.456 ± 0.003	0.015 ± 0.004	0.008 ± 0.002
B3	0.979 ± 0.008	2	0.166 ± 0.022	0.622 ± 0.002	0.130 ± 0.017	0.004 ± 0.002
			0.276 ± 0.035	0.729 ± 0.009	0.027 ± 0.006	0.064 ± 0.010

Notes. The parameters are defined in equation (1). We considered phase 0–0.3 for B1, 0.3–0.55 for B2, and 0.55–1.0 for B3. For different dips, f_0 is slightly different because of imperfect continuum normalization.

Table 3. Transit depth ratios at the observed wavelengths.

	D_{opt}	D_{K_s}	D_{K_s}/D_{opt}	$D_{4.5\,\mu m}$	$D_{4.5\,\mu m}/D_{opt}$
A1	1.000 ± 0.021	0.664 ± 0.034	0.664 ± 0.037	0.256 ± 0.032	0.256 ± 0.032
B2	1.000 ± 0.056	0.768 ± 0.057	0.768 ± 0.071	0.309 ± 0.073	0.309 ± 0.075
B3	1.005 ± 0.013	0.796 ± 0.018	0.792 ± 0.021	0.240 ± 0.026	0.239 ± 0.026
Average			0.741 ± 0.028		0.268 ± 0.029

Notes. D is the best-fitting parameter defined in equation (2). D_{opt} is not exactly unity because it depends on the range chosen to calculate the out-of-transit flux, which is different for the B2 and B3 dips. The uncertainty in D_{opt} illustrates a minimum uncertainty even when fitting the same data in different ways (with equations 1 and 2).

can be derived from white dwarf model calculations. We take the correction factor $F_{obs}/F_\star$ to be a constant.

We calculated white dwarf model spectra with parameters listed in Table 4 and derived the fact that the white dwarf flux is 53.5 μJy at K_s band and 13.0 μJy at 4.5 μm. Varying the temperature by 500 K and log g by 0.2 dex, we found the white dwarf flux could change by at most 2 per cent and we adopted that as the uncertainty of the intrinsic white dwarf flux. The measured total flux is 69.4 ± 5.2 μJy

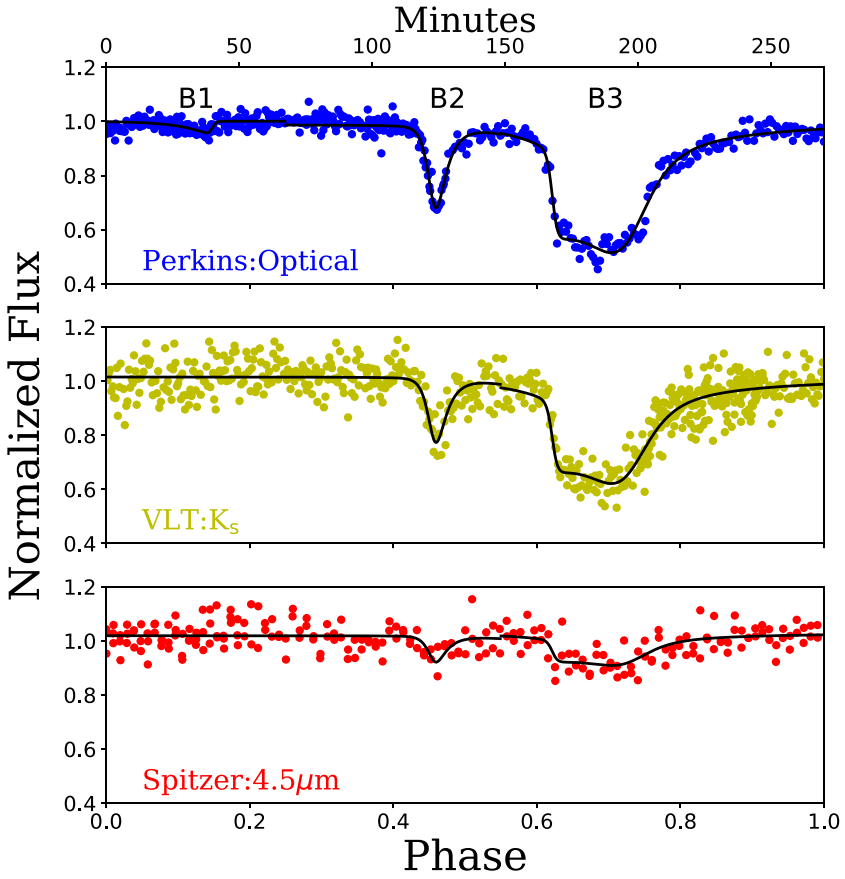

Figure 5. Similar to Fig. 4 except for the 2017 data set.

Table 4. WD 1145+017 system parameters.

Parameter	Symbol	Value	Reference
WD			
Effective temperature	$T_\star$	15 900 K	Vanderburg et al. (2015)
Surface gravity	log g	8.0	Vanderburg et al. (2015)
Distance	d	174 pc	Vanderburg et al. (2015)
Mass	$M_\star$	0.6 $M_\odot$	Dufour et al. (2017)
Radius	$R_\star$	0.013 $R_\odot$	Dufour et al. (2017)
Transiting material			
Orbital period	P	269.47 min	Gary et al. (2017)
Orbital distance	r	1.16 $R_\odot$	Kepler's third law

in K_s band from the UKIDSS and 55.0 ± 3.2 μJy at 4.5 μm, as derived in Section 2.3. Therefore, the correction factors are

$$\left(\frac{F_{\rm obs}}{F_\star}\right)_{K_s} = 1.30 \pm 0.10$$

$$\left(\frac{F_{\rm obs}}{F_\star}\right)_{4.5\,\mu{\rm m}} = 4.23 \pm 0.26.$$

Following equation (3), the corrected average transit depth ratios are

$$\left(\frac{D_{K_s}}{D_{\rm opt}}\right)_{\rm corr} = 0.96 \pm 0.08$$

$$\left(\frac{D_{4.5\,\mu{\rm m}}}{D_{\rm opt}}\right)_{\rm corr} = 1.13 \pm 0.14.$$

The corrected transit depths in K_s band and 4.5 μm are unexpectedly and even surprisingly consistent with the transit depth in the optical, at least to within the uncertainties. This result tends to indicate that the extinction cross-section is independent of wavelength for the observations from optical to 4.5 μm.

The main source of uncertainty for this analysis comes from the correction factor $F_{\rm obs}/F_\star$ in equation (3), which is mostly from the uncertainty of the absolute flux measurements. Currently, it is 7.5 per cent in K_s and 5.8 per cent at 4.5 μm. Future observations in the infrared will improve the flux measurement in K_s band. However, IRAC observations will always be limited by its absolute flux calibration, which is ∼5 per cent.

In the following section, we explore possible physical reasons for the wavelength independence of the transit depth.

4 CONSTRAINTS ON THE PARTICLE SIZE

The lack of a wavelength dependence of the transit depths could be expected if the dust clouds are optically thick. However, in order to explain both the transit depth and transit duration (e.g. the ∼20 per cent deep and ∼90 min long transit reported in Alonso et al. 2016), an opaque cloud needs to be both flat and also almost perfectly aligned with the orbital direction. We therefore consider opaque clouds to be an unlikely explanation for the transiting material around WD 1145+017.

An alternative explanation for the colour-independent transit depths is that large grains (i.e. $\gtrsim$1−2 μm) dominate the extinction cross-section of the clouds and their cross-sections are nearly independent of wavelength out to 4.5 μm.

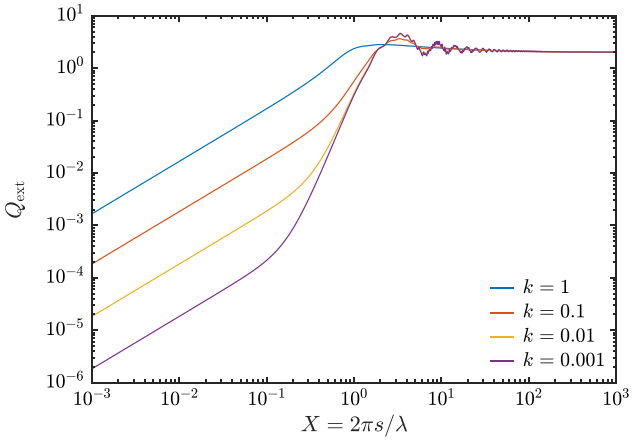

Figure 6. Extinction efficiency as a function of scaled particle size X for a range of grains with the real part of the index of refraction n being fixed at 1.6 and the imaginary part k between 0 and 1. For grains that satisfy $X \gtrsim 2$, $Q_{\rm ext}$ is independent of wavelength and remains a constant.

We explore the wavelength dependence of the extinction efficiency (the ratio of the extinction cross-section $\sigma_{\rm ext}(X)$ to the geometric cross-section), $Q_{\rm ext} \equiv \sigma_{\rm ext}(X)/\pi s^2$, where s is the particle radius, λ is the observing wavelength, and $X \equiv 2\pi s/\lambda$, the scaled particle size.[3] We adopted the Mie algorithm presented in Bohren & Huffman (1983) and the results for a range of generic materials are shown in Fig. 6. Similar to results from previous studies (e.g. Croll et al. 2014), we found that for very small values of $X(\lesssim 0.1)$, $Q_{\rm ext} \propto \lambda^{-1}$ is valid, while for large $X \gtrsim 2$, $Q_{\rm ext} \to 2$, i.e. independent of λ. For intermediate values of X, $Q_{\rm ext} \propto \lambda^{-4}$.

Since we find a colourless transit depth between $\lambda \simeq 0.5$ and 4.5 μm, we can reasonably infer that $X \gtrsim 2$ even at the longest wavelength of our observations. Specifically, we find that

$$X = \frac{2\pi s}{\lambda} \gtrsim 2 \tag{4}$$

Therefore, we tentatively conclude that our non-detection of wavelength-dependent transit depths from optical to 4.5 μm implies that the transiting material around WD 1145+017 must consist of grains whose sizes are largely $\gtrsim$1.5 μm.

We can also compare the transit depth ratios at different wavelengths with the corresponding Mie extinction cross-sections. We consider two generic grain materials (with $n = 1.6$ and $k = 0.1$, 0.01), and two particle size distributions.

Hansen distribution: for a range of characteristic particle sizes of $\bar{s} = 0.2, 0.5, 1, 2, 5, 10$ μm, the specific form of the distribution is (Hansen & Travis 1974)

$$n(s) = Cs^{(1-3b)/b} e^{-s/\bar{s}b},$$

where C is a normalization constant, s is the particle radius, and b is the dimensionless variance of the distribution. Following Zhou et al. (2016), we choose a value for b of 0.1, which provides a distribution that ranges from a factor of roughly $\sqrt{0.1}$ below $\bar{s}$ to a factor of $\sqrt{10}$ above $\bar{s}$. The normalized distribution is then

$$n(s) = \frac{1}{\Gamma(10)(0.1\bar{s})^{10}} s^7 {\rm e}^{-10s/\bar{s}}$$

[3] We note that this simple functional form for $Q_{\rm ext}$ can only be used when the imaginary part of the complex index of refraction is essentially independent of wavelength.

Cut-on power-law size distribution: we also consider a classical power-law distribution from a collisional cascade:

$$n(s) = Cs^{-3.5}, \tag{5}$$

where the minimum grain size $s_{\rm min}$ is fixed. This distribution is probably a more realistic representation of the particle size distribution as small grains may sublimate rapidly, as discussed in the next section. Note that in the cut-on power-law size distribution the effective particle size is larger than $s_{\rm min}$.

As shown in Fig. 7, we find that for both size distributions, only grains larger than $\gtrsim$2 μm can explain the observed transit depth ratios at the different wavelengths.

This minimum inferred grain size, for either choice of size distribution, is broadly consistent with the grain size derived from modelling the 10 μm silicate emission feature around other dusty white dwarfs (Jura, Farihi & Zuckerman 2009; Reach et al. 2009). On the other hand, small dust ($s \lesssim 1$ μm) is prevalent in the interstellar medium (e.g. Mathis, Rumpl & Nordsieck 1977), while in the Solar system the tails of comets and streams coming off the active asteroids can be a mixture of small and large grains (with s from sub-μm to cm), depending on the dust production mechanism (e.g. Jewitt 2012).

5 A POSSIBLE MODEL: GRAIN SUBLIMATION

In this section, we explore a physical explanation for the dearth of small grains in the transiting dust clouds. In summary, the explanation is that small grains have higher equilibrium temperatures than large grains, with the result that they are quickly destroyed by sublimation (see also von Hippel et al. 2007). The process of sublimation has an extremely steep dependence on temperature, so a modest increase in dust temperature can result in drastically shorter sublimation time-scales. To assess this scenario, we first compute the equilibrium temperature of dust grains in the transiting clouds (Section 5.1), then evaluate whether sublimation occurs in the potentially gas-rich circumstellar environment of WD 1145+017 (Section 5.2), and finally calculate dust sublimation time-scales as a function of grain size (Section 5.3). Throughout this analysis, we use the parameter values for the WD 1145+017 system listed in Table 4.

5.1 Dust temperatures

The temperature $T_{\rm d}(s, r)$ of a dust grain with radius s at distance r from the white dwarf can be calculated by solving the power balance between the incoming stellar radiation and the outgoing thermal radiation:

$$\frac{R_\star^2}{4r^2} \int Q_{\rm abs}(s,\lambda) B_\lambda(\lambda, T_\star)\, {\rm d}\lambda = \int Q_{\rm abs}(s,\lambda) B_\lambda(\lambda, T_{\rm d})\, {\rm d}\lambda. \tag{6}$$

The meanings for some symbols are listed in Table 4. $Q_{\rm abs}$ is the absorption efficiency of the dust grain, and B_λ is the Planck function. The white dwarf spectrum is approximated by blackbody radiation. This calculation ignores the latent heat of sublimation, which we find to be negligible (Rappaport et al. 2014).

The grain temperature depends critically on the absorption efficiency $Q_{\rm abs}$, which is generally a complicated function of grain size s, wavelength λ, and the optical constants of the dust material, i.e. its complex refractive index $n + {\rm i}k$. In certain cases, however, simple prescriptions for $Q_{\rm abs}$ can be derived, which allow the power balance equation (6) to be solved analytically (e.g. Backman & Paresce 1993; von Hippel et al. 2007).

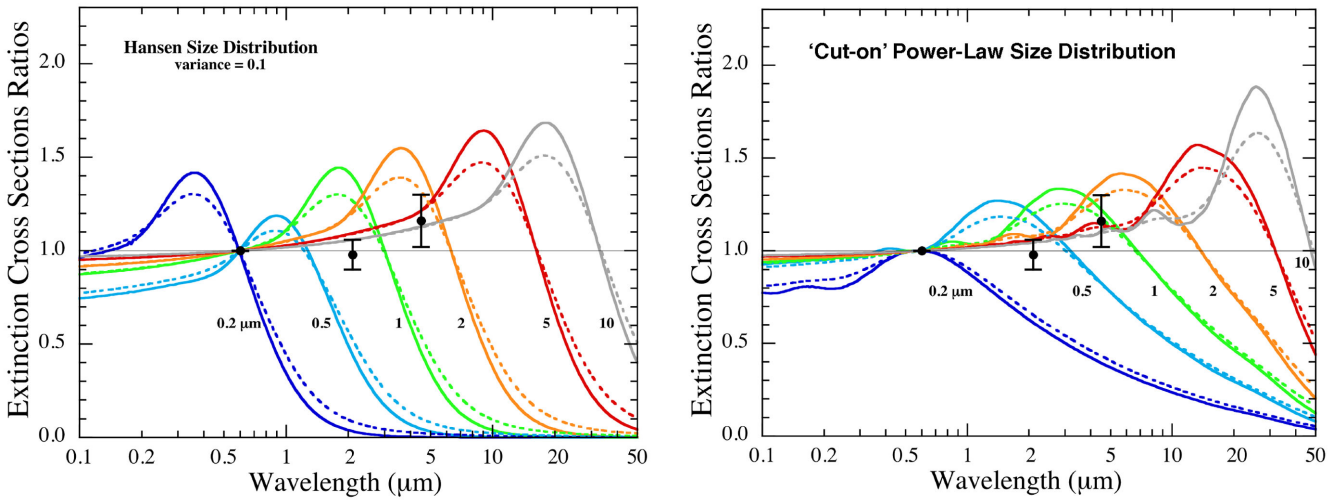

Figure 7. Mie extinction cross-sections at wavelength λ divided by the corresponding cross-section at 0.6 μm (optical) for a generic grain material, where n is set to be 1.6, and $k = 0.1$ (solid curves) and 0.01 (dashed curves). Two size distributions are shown. Left: Hansen distribution, where the labels represent the characteristic particle sizes. Right: a 'cut-on' power-law size distribution (see definition in equation 5), where the labels represent the minimum grain size $s_{\rm min}$. We also show the measured transit depth ratios in WD 1145+017 (black dots) as measured in this work. Only characteristic particle sizes of $\gtrsim$2 μm are consistent with the data.

For grains that are very large compared to the radiation wavelength, the absorption efficiency asymptotically approaches a constant value of $Q_{\rm abs} \approx 1$. In this limit, solving equation (6) gives the blackbody temperature

$$T_{\rm bb} = \sqrt{\frac{R_\star}{2r}}\, T_\star \approx 1.2 \times 10^3\,{\rm K} \times \left(\frac{T_\star}{15\,900\,{\rm K}}\right) \left(\frac{R_\star}{0.013\,{\rm R}_\odot}\right)^{1/2} \left(\frac{r}{1.16\,{\rm R}_\odot}\right)^{-1/2}. \quad (7)$$

For very small grains, which fall in the Rayleigh regime, $Q_{\rm abs} \propto \lambda^{-1}$ is found, which yields (e.g. Appendix C of Rappaport et al. 2014)

$$T_{\rm Rayl} = \left(\frac{R_\star}{2r}\right)^{2/5} T_\star \approx 2.0 \times 10^3\,{\rm K} \times \left(\frac{T_\star}{15\,900\,{\rm K}}\right) \left(\frac{R_\star}{0.013\,{\rm R}_\odot}\right)^{2/5} \left(\frac{r}{1.16\,{\rm R}_\odot}\right)^{-2/5}. \quad (8)$$

For general cases, the grain temperature can be found by solving equation (6) using $Q_{\rm abs}$ from the Mie theory (Bohren & Huffman 1983). In Fig. 8, we plot grain temperatures as a function of grain size. This shows the convergence towards the limiting temperatures for small and large grain sizes. Small grains can reach a much higher temperature of 2000 K than large grains of 1200 K. Interestingly, for dust orbiting WD 1145+017 in a 4.5 h period, the values of the two limiting temperatures bracket the temperatures at which many refractory materials sublimate rapidly.

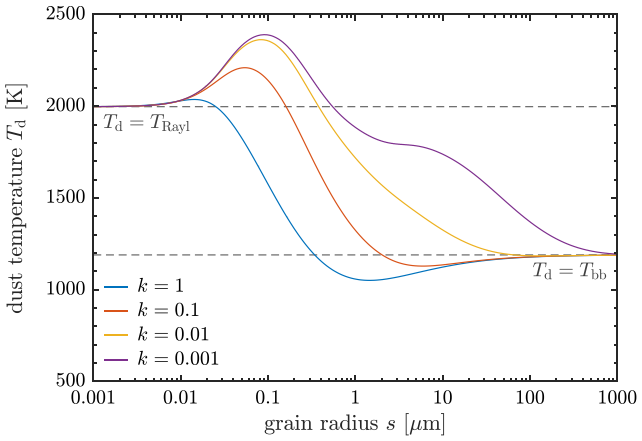

Figure 8. Temperature as a function of grain size for dust grains in orbit around WD 1145+017 at 4.5 h. The solid coloured lines represent generic minerals with different values of k, the imaginary part of the index of refraction. The real part is kept fixed at $n = 1.6$. Also shown are the two limiting cases of Rayleigh-approximation and blackbody temperatures (dashed horizontal lines). Small grains are heated to a higher temperature than large grains.

5.2 The sublimation/condensation balance

Like all thermodynamic phase transitions, sublimation depends on the pressure and temperature of the matter involved, and the balance between sublimation and condensation can be evaluated using a phase diagram. For a given temperature T, the pressure at which these two processes are in equilibrium is called the phase-equilibrium (or saturated) vapour pressure $p_{\rm sat}$. Based on the Clausius–Clapeyron relation, its temperature dependence is found to be

$$p_{\rm sat}(T) = \exp(-\mathcal{A}/T + \mathcal{B})\ {\rm dyn\,cm^{-2}}, \quad (9)$$

where $\mathcal{A}$ and $\mathcal{B}$ are material-dependent sublimation parameters that can be determined experimentally. Dust grains with temperature $T_{\rm d}$ will sublimate when the ambient gas pressure $p_{\rm g}$ is lower than $p_{\rm sat}(T_{\rm d})$, while condensation happens for $p_{\rm g} > p_{\rm sat}(T_{\rm d})$.

To assess whether sublimation or condensation dominates, we make a rough estimate of the ambient gas pressure. Assuming the gas around the white dwarf forms a steady-state viscous accretion disc, where the viscosity is parametrized by α_ν, the gas pressure in

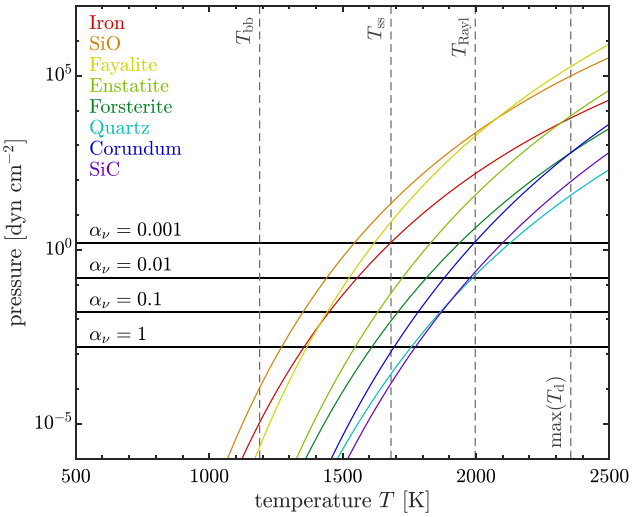

Figure 9. Phase-equilibrium vapour pressure $p_{\rm sat}$ as function of temperature for a set of possible dust species from equation (9) (coloured lines), together with estimates of the ambient gas pressure $p_{\rm g}$ for several different values of the viscosity parameter α_ν from equation (10) (horizontal black lines). Sublimation occurs when $p_{\rm g} < p_{\rm sat}$, while condensation happens when $p_{\rm g} > p_{\rm sat}$. Also indicated are temperatures reached by particles orbiting WD 1145+017 in several limiting cases (dashed vertical lines): $T_{\rm bb}$, the blackbody temperature valid for large dust grains; $T_{\rm ss}$, the temperature at the substellar point of a tidally locked large body (based on equation 5 in Vanderburg et al. 2015); $T_{\rm Rayl}$, the limiting temperature for small grains; and max ($T_{\rm d}$), the maximum dust temperature seen in Fig. 8.

the disc is given approximately by (Rafikov & Garmilla 2012)

$$p_{\rm g} = \frac{\dot{M}\Omega_{\rm K}^2}{3\pi\alpha_\nu c_{\rm s}} \approx 0.2\,{\rm dyn\,cm^{-2}} \times \left(\frac{\dot{M}}{10^{10}\,{\rm g\,s^{-1}}}\right)\left(\frac{P}{4.5\,{\rm h}}\right)^{-2}\left(\frac{\alpha_\nu}{0.01}\right)^{-1}\left(\frac{c_{\rm s}}{1\,{\rm km\,s^{-1}}}\right)^{-1}. \quad (10)$$

Here, $\Omega_{\rm K}$ is the local Keplerian angular frequency and $c_{\rm s}$ is the sound speed. The mass accretion rate $\dot{M}$ can be estimated from pollution in the white dwarf's atmosphere, assuming a steady state accretion (Xu et al. 2016). In addition, $c_{\rm s} \sim 1\,{\rm km\,s^{-1}}$ is a reasonable estimate for the sound speed of a metallic gas with a temperature of a few thousand K, so the uncertainty in $p_{\rm g}$ is dominated by the poor knowledge of α_ν. Note that the temperature and vertical distribution of the gaseous disc can be substantially different from that of the dust (section 6 in Melis et al. 2010).

Fig. 9 shows a comparison of the phase-equilibrium vapour pressures of a set of possible refractory materials, excluding graphite[4] (using values of $\mathcal{A}$ and $\mathcal{B}$ in table 3 of van Lieshout, Min & Dominik 2014) with the estimated ambient gas pressure associated with the presumed gaseous accretion disc. Although there is great uncertainty in both $p_{\rm sat}$ (because the dust composition is not well constrained) and $p_{\rm g}$ (because α_ν is unknown), the figure reveals that sublimation is expected for dust with temperatures around $T_{\rm Rayl}$ (small grains), while material with temperatures around $T_{\rm bb}$ (large grains) could be protected from sublimation by the gas disc.

[4] Graphite is unlikely to be the dominant component of the dust particles because carbon has not yet been detected in the atmosphere of WD 1145+017 (Xu et al. 2016). In fact, almost all polluted white dwarfs are carbon-depleted (e.g. Jura 2006). Graphite is excluded for all the following analyses.

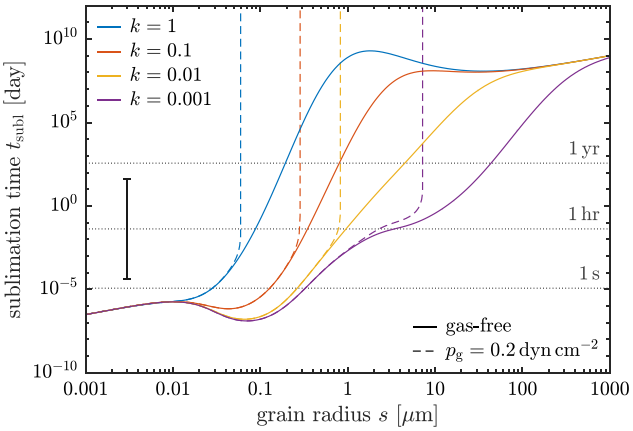

Figure 10. Sublimation time-scale as function of grain size assuming the dust temperatures from Fig. 8 and sublimation parameters corresponding to a generic refractory material. Different coloured lines correspond to different values of the imaginary part of the complex refractive index k. The real part is kept fixed at $n = 1.6$. The solid curves are for dust grains in vacuum; the dashed curves assume an ambient gas density of $p_{\rm g} \approx 0.2\,{\rm dyn\,cm^{-2}}$ (see Section 5.2). The error bar is a rough indication of the uncertainty in sublimation time found by considering different possible dust materials (specifically, those listed in Fig. 9).

5.3 A minimum grain size due to sublimation

Because the Rayleigh-approximation temperature is higher than the blackbody temperature ($T_{\rm Rayl}/T_{\rm bb} \approx 1.7$), the dust temperature must go up with decreasing grain size. Dust sublimation rates have an extremely steep dependence on temperature, so this increase in temperature will be associated with a dramatic decrease in dust survival time against sublimation. In contrast, when the dust temperature is constant with grain size, the sublimation time-scale will only decrease linearly with decreasing grain size.

To quantify the effect of sublimation on grain survival times, we compute dust sublimation time-scales, given by

$$t_{\rm subl} = -\frac{s}{\dot{s}} = \frac{s\rho_{\rm d}}{J(T_{\rm d})}. \quad (11)$$

Here, s is the grain radius, $\dot{s}$ is its change rate, $\rho_{\rm d}$ is the density of the dust material, and J is the net sublimation mass-loss flux (units: [g cm^{-2} s^{-1}]; positive for mass-loss). The mass-loss flux J can be calculated from the kinetic theory of gasses (e.g. Langmuir 1913):

$$J(T) = \alpha_{\rm subl}\left[p_{\rm sat}(T) - p_{\rm g}\right]\sqrt{\frac{\mu {\rm m_u}}{2\pi k_{\rm B} T}}. \quad (12)$$

Here, $\alpha_{\rm subl}$ is the evaporation coefficient, also known as the 'accommodation coefficient' or 'sticking efficiency', which parametrizes kinetic inhibition of the sublimation process (which we assume to be independent of temperature), μ is the molecular weight of the molecules that sublimate, $m_{\rm u}$ is the atomic mass unit, and $k_{\rm B}$ is the Boltzmann constant.

In Fig. 10, we show the sublimation time-scale as a function of grain size using dust temperatures computed in Section 5.1. The calculation uses a set of sublimation parameters typical for a generic refractory material: $\mathcal{A} = 65\,000$ K, $\mathcal{B} = 35$, $\rho_{\rm d} = 3\,{\rm g\,cm^{-3}}$, $\alpha_{\rm subl} = 0.1$, and $\mu = 100$. These fall roughly in the middle of the range of values seen for the refractory materials shown in Fig. 9 (see van Lieshout et al. 2014).

Fig. 10 demonstrates that small dust is destroyed almost instantaneously, while large dust could survive against sublimation for many years. This result is robust despite the large uncertainty in

sublimation time-scale introduced by the uncertainty in dust composition and hence sublimation parameters (there are about two to four orders of magnitude spread in sublimation time-scale amongst the materials shown in Fig. 9). We conclude that the large grain sizes inferred from the lack of wavelength dependence in the transit depths of WD 1145+017 is likely the result of sublimation of smaller grains, because of their higher equilibrium temperatures and rapid sublimation. This conclusion holds when considering both gas-free and gas-rich environments. In the gas-free case, large grains have very long sublimation time-scales, and their lifetime is likely set by other destruction processes than sublimation. In the gas-rich case, large grains are also protected from sublimation by the gas disc (as discussed in Section 5.2).

Our method of estimating sublimation time-scales assumes the temperature of the dust grain to remain constant as it decreases in size due to sublimation, which is incorrect as shown in Fig. 8. However, given the extreme temperature dependence of the sublimation process, the sublimation time-scale will be dominated by the lowest dust temperatures encountered. Hence, equation (11) using the initial dust temperature provides a very good estimate of the sublimation time-scale.

The exact value of the grain size s below which sublimation destroys grains faster than they are replenished depends on a number of factors: the optical properties of the dust (most importantly the value of the imaginary part of the complex refractive index k); its sublimation parameters (i.e. $\mathcal{A}$, $\mathcal{B}$, $\alpha_{\rm subl}$, μ, and $\rho_{\rm d}$); the time-scale on which other processes (like collisions) destroy dust grains when the sublimation time-scale is long; and the size-dependent input rate of dust, which is determined by the dust production process and is still unknown. By modelling the resultant grain size distribution, it is in principle possible to use the lower limit on the minimum grain size inferred from the observation to put constraints on the composition of the dust. This exercise is beyond the scope of this work, but will be the subject of a future study. For now, we tentatively suggest that the inferred lower limit of $s \gtrsim 1.5$ μm disfavours metallic dust species like pure iron.[5] The reason is that these materials typically have $k > 1$ (i.e. they are reflective) and grains smaller than 1 μm can survive for a considerable amount of time before sublimation, as shown in Fig. 10.

6 INFRARED EXCESS AND THE TRANSITING MATERIAL

WD 1145+017 displays excess infrared radiation starting from the $K_{\rm s}$ band. There are over 40 known dusty white dwarfs (Farihi 2016) and usually, they have been modelled with a geometrically thin, optically thick dust disc within the white dwarf's tidal radius (Jura 2003). The sublimation/condensation calculation presented in Section 5 can also be relevant for the innermost region of the dust discs, where the dust is optically thin and directly exposed to the radiation from the white dwarf. However, the detailed process is highly dependent on the density and viscosity of the surrounding metallic gas (e.g. Rafikov 2011). Occasionally, the infrared excess is so strong that a warped disc is preferred (Jura et al. 2007a,b). As shown in Fig. 11, the fractional luminosity of the infrared excess around WD 1145+017 is comparable to other white dwarfs with a dust disc. There is a general trend of increasing fractional luminosity as the white dwarf cools, which points to a possible disc evolution sequence (Rocchetto et al. 2015).

[5] In spite of this conclusion, we note that Fe is abundant in the atmosphere of WD 1145+017 (Xu et al. 2016).

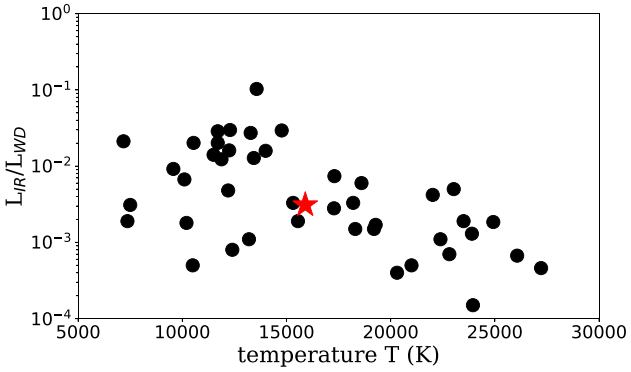

Figure 11. Fractional luminosity of the infrared excess for all known dusty white dwarfs versus the effective temperature. The red star represents WD 1145+017, whose fractional IR luminosity is typical of dusty white dwarfs at this temperature range.

Table 5. Best-fitting parameters to the SED of WD 1145+017.

Model	$\chi^2_{\rm d}$	Parameters
disc1	1.3	$R_{\rm in} = 13R_\star$, $R_{\rm out} = 120R_\star$, $\cos i = 0.18$
		$T_{\rm in} = 1570$ K, $T_{\rm out} = 300$ K
disc2	2.5	$R_{\rm in} = 19R_\star$, $R_{\rm out} = 25R_\star$, $\cos i = 0.80$
		$T_{\rm in} = 1190$ K, $T_{\rm out} = 970$ K
Blackbody	1.3	$T_{\rm bb} = 1150$ K, $A = 160\pi R_\star^2$

Notes. We fit four data points, including fluxes from H, $K_{\rm s}$, W-1, and IRAC-2. $\chi^2_{\rm d}$ is calculated for per degree of freedom, which is 1 for the opaque disc model and 2 for the blackbody model. For disc1, the outer radius $R_{\rm out}$ is not well constrained due to the lack of longer wavelength observations. We kept it at $120R_\star$, the typical tidal radius of white dwarfs.

The *Spitzer* IRAC-2 measurement of 55.0 ± 3.2 μJy at 4.5 μm greatly reduced the uncertainty compared to the WISE-2 measurement of 43 ± 14 μJy (see Section 2.3). Here, we explore the spectral energy distribution (SED) fits of WD 1145+017 with two simple models.

(i) *A flat opaque disc.* We follow the classical recipe of fitting opaque dust discs around white dwarfs from Jura (2003) with three free parameters, the inner radius of the disc $R_{\rm in}$, outer radius of the disc $R_{\rm out}$, and inclination $\cos i$. There is a degeneracy between the surface area of the dust disc and its inclination. We performed chi-squared minimizations to find the best-fitting parameters for two extreme cases, i.e. with large and small inclinations, as listed in Table 5 and also shown in Fig. 12. For model 'disc1', the inner radius corresponds to a temperature similar to the inner disc temperature of other dusty white dwarfs, likely determined by sublimation and the outer radius is located near the tidal radius. Model 'disc2' is effectively a face-on narrow ring close to the white dwarf. Its SED is very similar to that of a blackbody. To produce the observed infrared excess with a flat opaque disc, the disc would not be aligned with the transiting objects. Under this scenario, either the dust disc and the transiting objects come from different parent bodies with different orbital inclination, or some additional mechanism is required to perturb the dust disc to be misaligned with the transiting objects.

(ii) *An inflated optically thin disc.* The best-fitting blackbody model has an effective temperature of 1150 K and surface area of $160\pi R_\star^2$, which is consistent with the numbers derived in Vanderburg et al. (2015). This temperature is comparable to the temperature

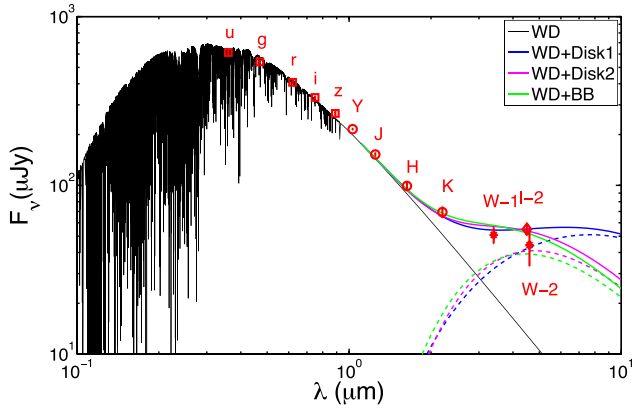

Figure 12. SED fits of the infrared excess around WD 1145+017. The red square, circle, star, and diamond symbols represent measurement from the SDSS, UKIDSS, *WISE*, and *Spitzer*, respectively. The black line represents flux from the white dwarf model. The blue and magenta dashed lines represent flux from an opaque disc with parameters listed in Table 5 while the blue dashed line represents flux from a blackbody. The solid coloured lines represent flux from the white dwarf plus an additional component, either a disc or a blackbody.

of large grains around the transiting material at 1.16 $R_\odot$ (90 $R_\star$), as derived in equation (7). To produce the observed infrared excess, a disc height of 0.9 $R_\star$ is required. Collisional cascades around the Roche limits of white dwarfs have been studied recently in Kenyon & Bromley (2017). They found that for discs made of indestructible particles, the scale height would quickly reduce to a value that is comparable to the particle radius. However, with additional mass input, the scale height of the dust disc can remain quite high for a long time. This is a viable alternative because there is a constant mass input from the disintegrating material into the dust disc around WD 1145+017. In addition, from the deep transits in the light curve, we know that the transiting material has significant height as well. A prediction from this model is that the disc scale height is dependent on the mass input rate. It is essential to keep monitoring the infrared flux of the dust disc to look for any variations correlated with the transit light curve.

It is worth noting that the transiting material could contribute to the infrared excess as well. We approximate the total effective surface area of the dust as a cylinder and it can be calculated as

$$A \approx 2\pi r \times \epsilon \times \delta \times \sqrt{\pi} R_\star, \quad (13)$$

where ϵ is the percentage of time a transit lasts, δ is the average transit depth, both can be estimated from the light curve and $\sqrt{\pi}R_\star$ represents the effective height of the stellar disc. For the 2016 data set, we found $\epsilon = 0.22$ and $\delta = 0.17$. For the 2017 data set, for B2, $\epsilon = 0.10$, $\delta = 0.09$ while for B3, $\epsilon = 0.25$, $\delta = 0.33$. The total surface area of the transiting material is $\sim 12\pi R_\star^2$ and $\sim 29\pi R_\star^2$ in 2016 and 2017, respectively. Thus, there is an increase in surface area by a factor of 2.5 in the 2017 light curve compared to the 2016 light curve. However, the surface area of the transiting material is still relatively small compared to the total inferred surface area of the emitting dust of $160\pi R_\star^2$, and the 4.5 μm flux remains constant between 2016 and 2017 observations, requiring a long lasting reservoir of ∼1200 K dust. Regardless, there could be a significant fraction of non-transiting dust material and the sublimation time-scale for large particle is years or longer, as shown in Fig. 10. The transiting objects could supply material for the observed infrared excess.

7 SUMMARY AND CONCLUSION

We have presented two epochs of multiwavelength photometric observations of WD 1145+017, covering from optical to 4.5 μm during 2016 March 28–29 and 2017 April 4–5. One main transit feature was detected in 2016 and three transit features in 2017 during a 4.5 h orbital period. We modelled the transit features and found that the observed transit depths were different at all the observed wavelengths. After correcting for the excess infrared emission from orbiting dust particles in the K_s and 4.5 μm bands, we found that the transit depths are the same from optical to 4.5 μm during both epochs.

This wavelength-independent transit behaviour can be explained by a dearth of small grains ($\lesssim$1.5 μm) in the transiting material. Small grains are heated to a higher temperature than large grains. In addition, sublimation rates have a steep dependence on grain temperature. As a result, we suggest a model where small grains sublimate rapidly and only large grains can survive long enough to be detectable.

The dust released from the hypothesized orbiting bodies will continually add mass into the circumstellar dust, which could potentially maintain a large scale height. We present two models that can equally fit the infrared excess of WD 1145+017, including a flat opaque disc and an inflated optically thin disc. Future observations, particularly monitoring in the infrared, will improve our understanding of the link between the transiting material and the infrared excess.

Note added in manuscript: After this work was substantially complete, we became aware of an interesting model by Farihi, von Hippel & Pringle (2017) that might explain some of the properties of the peculiar transits in WD 1145+017. This model involves magnetic entrainment of small ($a \sim 0.1$ μm) charged particles in the field of a strongly magnetized white dwarf. In the context of either the Farihi et al. (2017) scenario, or the one we have assumed, namely dust clouds released by orbiting bodies with periods near 4.5 h, all of the measured transit depths and dust size determinations made in this work should still be equally valid. All of the calculations we made suggesting that the smaller dust grains should sublimate quickly would remain unchanged in either scenario. Thus, none of our conclusions should be affected.

ACKNOWLEDGEMENTS

We thank the *Spitzer* helpdesk for useful discussions about high-precision photometry. The paper was based on observations made with (i) the *Spitzer Space Telescope* under programme no. 12128 and no. 13065, which is operated by the Jet Propulsion Laboratory, California Institute of Technology under a contract with National Aeronautics and Space Administration (NASA). Support for this work was provided by NASA through an award issued by JPL/Caltech. (ii) The European Organisation for Astronomical Research in the Southern Hemisphere under European Southern Observatory (ESO) programme 296.C-5024 and 099.C-0082. This work also uses observations from the Las Cumbres Observatory (LCO) network. RvL acknowledges support from the European Union through ERC grant numbers 279973 and 341137. AC acknowledges support from STFC grant ST/M001296/1.

REFERENCES

Alonso R., Rappaport S., Deeg H. J., Palle E., 2016, A&A, 589, L6
Backman D. E., Paresce F., 1993, in Levy E. H., Lunine J. I., eds, Protostars and Planets III. Univ. Arizona Press, Tucson, p. 1253

Bohren C. F., Huffman D. R., 1983, Absorption and Scattering of Light by Small Particles. Wiley, New York
Brinkworth C. S., Gänsicke B. T., Marsh T. R., Hoard D. W., Tappert C., 2009, ApJ, 696, 1402
Brown T. M. et al., 2013, PASP, 125, 1031
Cáceres C. et al., 2011, A&A, 530, A5
Collins K., Kielkopf J., 2013, Astrophysics Source Code Library, record ascl:1309.001
Collins K. A., Kielkopf J. F., Stassun K. G., Hessman F. V., 2017, AJ, 153, 77
Croll B. et al., 2014, ApJ, 786, 100
Croll B. et al., 2017, ApJ, 836, 82
Dalba P. A., Muirhead P. S., 2016, ApJ, 826, L7
Dalba P. A., Muirhead P. S., Croll B., Kempton E. M.-R., 2017, AJ, 153, 59
Debes J. H., Sigurdsson S., 2002, ApJ, 572, 556
Dufour P., Blouin S., Coutu S., Fortin-Archambault M., Thibeault C., Bergeron P., Fontaine G., 2017, in Tremblay P.-E., Gaensicke B., Marsh T., eds, ASP Conf. Ser. Vol. 509, 20th European White Dwarf Workshop. Astron. Soc. Pac., San Francisco, p. 3
Farihi J., 2016, New Astron. Rev., 71, 9
Farihi J., Jura M., Zuckerman B., 2009, ApJ, 694, 805
Farihi J., von Hippel T., Pringle J. E., 2017, MNRAS, 471, L145
Fazio G. G. et al., 2004, ApJS, 154, 10
Gänsicke B. T., Marsh T. R., Southworth J., Rebassa-Mansergas A., 2006, Science, 314, 1908
Gänsicke B. T. et al., 2016, ApJ, 818, L7
Gary B. L., Rappaport S., Kaye T. G., Alonso R., Hambschs F.-J., 2017, MNRAS, 465, 3267
Grillmair C. J. et al., 2012, in Peck A. B., Seaman R. L., Comeron F., eds, Observatory Operations: Strategies, Processes, and Systems IV. SPIE, Bellingham, p. 84481I
Gurri P., Veras D., Gänsicke B. T., 2017, MNRAS, 464, 321
Hallakoun N. et al., 2017, MNRAS, 469, 3213
Hansen J. E., Travis L. D., 1974, Space Sci. Rev., 16, 527
Janes K. A., Clemens D. P., Hayes-Gehrke M. N., Eastman J. D., Sarcia D. S., Bosh A. S., 2004, American Astronomical Society Meeting Abstracts #204, Bulletin of the American Astronomical Society. Vol. 36, First Results from the Perkins Re-Imaging SysteM (PRISM), p. 672
Jewitt D., 2012, AJ, 143, 66
Jura M., 2003, ApJ, 584, L91
Jura M., 2006, ApJ, 653, 613
Jura M., Young E. D., 2014, Annu. Rev. Earth Planet. Sci., 42, 45
Jura M., Farihi J., Zuckerman B., Becklin E. E., 2007a, AJ, 133, 1927
Jura M., Farihi J., Zuckerman B., 2007b, ApJ, 663, 1285
Jura M., Farihi J., Zuckerman B., 2009, AJ, 137, 3191
Kenyon S. J., Bromley B. C., 2017, ApJ, 844, 116
Koester D., Gänsicke B. T., Farihi J., 2014, A&A, 566, A34
Langmuir I., 1913, Phys. Rev., 2, 450
Mathis J. S., Rumpl W., Nordsieck K. H., 1977, ApJ, 217, 425
Melis C., Jura M., Albert L., Klein B., Zuckerman B., 2010, ApJ, 722, 1078
Pirard J.-F. 2004, in Moorwood A. F. M., Iye M., eds, Proc. SPIE Conf. Ser. Vol. 5492, Ground-based Instrumentation for Astronomy. SPIE, Bellingham, p. 1763
Provencal J. L. et al., 2012, ApJ, 751, 91
Rafikov R. R., 2011, MNRAS, 416, L55
Rafikov R. R., Garmilla J. A., 2012, ApJ, 760, 123
Rappaport S. et al., 2012, ApJ, 752, 1
Rappaport S., Barclay T., DeVore J., Rowe J., Sanchis-Ojeda R., Still M., 2014, ApJ, 784, 40
Rappaport S., Gary B. L., Kaye T., Vanderburg A., Croll B., Benni P., Foote J., 2016, MNRAS, 458, 3904
Rappaport S., Gary B. L., Vanderburg A. et al., 2018, MNRAS, 474, 933
Reach W. T., Lisse C., von Hippel T., Mullally F., 2009, ApJ, 693, 697
Redfield S., Farihi J., Cauley P. W., Parsons S. G., Gänsicke B. T., Duvvuri G. M., 2017, ApJ, 839, 42
Rocchetto M., Farihi J., Gänsicke B. T., Bergfors C., 2015, MNRAS, 449, 574
van Lieshout R., Min M., Dominik C., 2014, A&A, 572, A76
Vanderburg A., Rappaport S., 2018, Transiting Disintegrating Planetary Debris around WD 1145+017. Springer-Verlag, Berlin
Vanderburg A. et al., 2015, Nature, 526, 546
Veras D., Carter P. J., Leinhardt Z. M., Gänsicke B. T., 2017, MNRAS, 465, 1008
von Hippel T., Kuchner M. J., Kilic M., Mullally F., Reach W. T., 2007, ApJ, 662, 544
Xu S., Jura M., Dufour P., Zuckerman B., 2016, ApJ, 816, L22
Zhou G. et al., 2016, MNRAS, 463, 4422
Zuckerman B., Koester D., Reid I. N., Hünsch M., 2003, ApJ, 596, 477
Zuckerman B., Koester D., Melis C., Hansen B. M., Jura M., 2007, ApJ, 671, 872
Zuckerman B., Melis C., Klein B., Koester D., Jura M., 2010, ApJ, 722, 725

APPENDIX A: OPTICAL LIGHT CURVE COMPARISON

In support of the *Spitzer* observation on 2017 April 4 and 5, we requested observing time in 10 optical telescopes all around the world. These 10 ground-based light curves offer a unique opportunity for assessing the level of systematics that can be expected in any single light curve. The observations are summarized in Table A1. These 10 observing sessions spanned 26 h, or ∼6 WD 1145+017 orbital periods, as shown in Fig. A1.

Most of the data were reduced with ASTROIMAGEJ, an open software for high-precision light curve extrapolations (Collins & Kielkopf 2013; Collins et al. 2017). The Las Cumbres Observatory (LCO) data were reduced following previous procedures developed for LCO observations of WD 1145+017 outlined in Zhou et al. (2016). The data reduction procedures for the JBO and HAO observations were described in Rappaport et al. (2016). The Perkins observations were described in detail in Section 2.1. All the light curves are shown in Figs A2 and A3, also shown is the best-fitting model for the *Perkins* data.

There are three main dip features in an orbital period, which we name B1, B2, and B3, respectively. Since the transits around WD 1145+017 change gradually, any noticeable change typically occurs on a longer time-scale than an orbital period. We consider the first three light curves as close enough in time to justify a direct comparison. The last seven light curves are simultaneous. We will refer to those two groups as 'early group' and 'late group'.

The early group of light curves were all obtained with the 1-m LCO network (Brown et al. 2013). The variations among the light curves suggest that systematic plus stochastic differences amount to ∼2.5 per cent for these data for a cadence ∼220 s. B1 has a depth about 2.7 per cent (see Table 2), and it was not detected in the LCO light curve. For the late group, the Perkins data have the best quality followed by the FLWO KeplerCam data.

As shown in Figs A2 and A3, the overall agreement is quite good during the 26 h, particularly for Dip B2 and B3. Dip B1 is isolated but it is the shallowest dip, and it is not well detected with smaller telescopes.

One main conclusion from this exercise is that in terms of observing a faint star like WD 1145+017, 'bigger is better'. The big telescopes are good for capturing short time-scale structure, whereas the small telescopes average over this structure. Fortunately, all telescopes measure the same overall structure and the depths of the dips, which we measure in this paper, are highly consistent among the different data sets.

Table A1. Summary of optical observations on 2017 April 4 and 5.

Telescope name	Location	Aperture	Observers	Cadence	Filters
		Early group			
LCO/COJ	SSO, Australia	1 m	Avi Shporer	221 s	*g*
LCO/LSC	CTIO, Chile	1 m	Avi Shporer	219 s	*g*
LCO/CPT	SAAO, South Africa	1 m	Avi Shporer	220 s	*g*
		Late group			
Perkins	Lowell, AZ	1.8 m	Paul Dalba	51 s	*R*
FLWO	FLWO, AZ	1.2 m	Allyson Bieryla	77 s	*V*
BYU	West Mountain Observatory, UT	0.91 m	Michael Joner	190 s	*V*
GMU	Fairfax, VA	0.81 m	Jenna Cann, Peter A. Panka	133 s	Clear
JBO	Hereford, AZ	0.81 m	Tom Kaye	58 s	Clear
ULMT	Mt. Lemmon, AZ	0.6 m	Karen Collins	213 s	Clear
HAO	Hereford, AZ	0.35 m	Bruce Gary	87 s	Clear

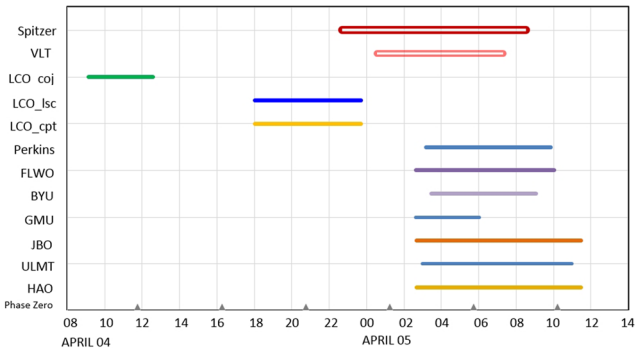

Figure A1. Observing times for 10 optical sessions in 2017. The details of the observation are listed in Table A1. The *Spitzer* and *VLT* observing windows are also shown for comparison. The triangles indicate phase zero, as defined in the text.

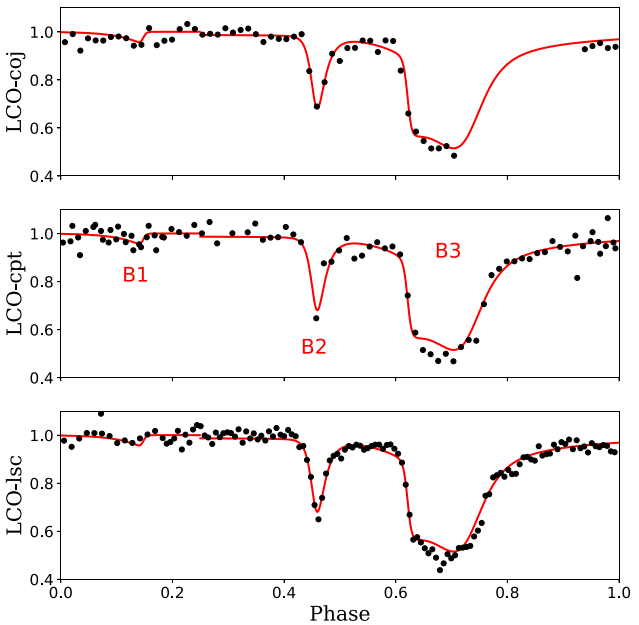

Figure A2. Comparison of the three light curves in the early group. The red line represents the best-fitting model for the Perkins data, as described in Section 3.1. All three light curves have a deeper B3 dip than the Perkins model, which is likely due to evolution of the transit shape over time.

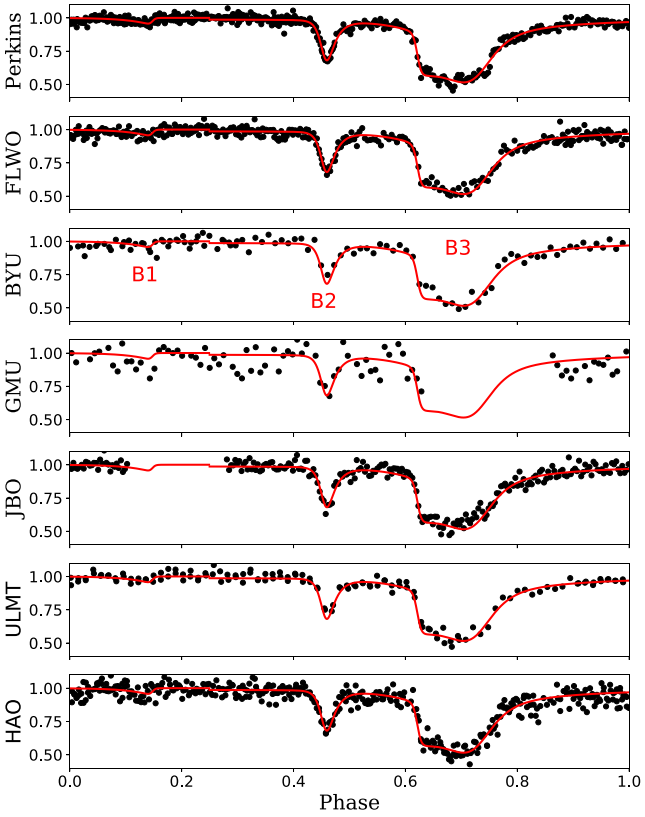

Figure A3. Comparison of the seven light curves in the late group. The red line represents the best-fitting model for the *Perkins* data, as described in Section 3.1.

[1]*European Southern Observatory, Karl-Schwarzschild-Straße 2, D-85748 Garching, Germany*
[2]*Department of Physics, Kavli Institute for Astrophysics and Space Research, Massachusetts Institute of Technology, Cambridge, MA 02139, USA*
[3]*Institute of Astronomy, University of Cambridge, Madingley Road, Cambridge CB3 0HA, UK*
[4]*Harvard-Smithsonian Center for Astrophysics, 60 Garden Street, Cambridge, MA 02138 USA*
[5]*Hereford Arizona Observatory, Hereford, AZ 85615, USA*
[6]*School of Physics and Astronomy, Tel-Aviv University, Tel-Aviv 6997801, Israel*
[7]*European Southern Observatory, Ave. Alonso de Córdova 3107, Vitacura, 7591538 Santiago, Chile*
[8]*Visidyne Inc., Santa Barbara, CA 93105, USA*

[9]*Observatoire Astronomique de l'Universit'e de Geneve, 51 ch. des Maillettes, CH-1290 Versoix, Switzerland*
[10]*Research School of Astronomy and Astrophysics, Mount Stromlo Observatory, Australian National University, Weston, ACT 2611, Australia*
[11]*Centre for Exoplanet Science, SUPA School of Physics and Astronomy, University of St Andrews, North Haugh, St Andrews KY16 9SS, UK*
[12]*Department of Physics and Astronomy, George Mason University, Fairfax, 22030 Virginia, USA*
[13]*Institute for Astrophysical Research, Boston University, 725 Commonwealth Avenue, Room 506, Boston, MA 02215, USA*
[14]*Space Telescope Science Institute, Baltimore, MD 21218, USA*
[15]*Paul and Jane Meyer Observatory, Coryell County, 76689 TX, USA*
[16]*Département de physique, Institut de Recherche sur les Exoplanètes (iREx) and Université de Montréal, Montréal, QC H3C 3J7, Canada*
[17]*Eureka Scientific Inc., Oakland, CA 94602, USA*
[18]*Instituto de Astrofísica, Facultad de Física, Pontificia Universidad Católica de Chile, Av. Vicuña Mackenna 4860, 782-0436 Macul, Santiago, Chile*
[19]*Department of Physics and Astronomy, Brigham Young University, Provo, UT 84602, USA*
[20]*Department of Physics and Astronomy, University of California, Los Angeles, CA 90095-1562, USA*
[21]*Chemistry and Physical Science Department, Raemor Vista Observatory, 7023 E. Alhambra Dr., Sierra Vista, AZ 85650, USA*
[22]*Temple College, Temple, TX 76504, USA*
[23]*Instituto de Astrofísica de Canarias, Calle Vía Láctea s/n, E-38205 La Laguna, Tenerife, Spain*
[24]*Departamento de Astrofísica, Universidad de La Laguna, Avda. Astrofísico Francisco Sánchez s/n, E-38206 La Laguna, Tenerife, Spain*
[25]*Department of Physics and Astronomy, University of Delaware, Newark, DE 19716, USA*
[26]*South African Astronomical Observatory, PO Box 9, Observatory, Cape Town 7935, South Africa*
[27]*Division of Geological and Planetary Sciences, California Institute of Technology, Pasadena, CA 91125, USA*

This paper has been typeset from a TEX/LATEX file prepared by the author.